Acta Astronautica 115 (2015) 121–137

Contents lists available at ScienceDirect

Acta Astronautica

journal homepage: www.elsevier.com/locate/actaastro

Review

Lessons learned from the dynamical behaviour of orbiting satellites

Jozef C. van der Ha

Satellite Mission Design and Operations, 5808 Bell Creek Road, Deming, WA 98244, USA

ARTICLE INFO

Article history:
Received 27 April 2015
Accepted 28 April 2015
Available online 9 May 2015

Keywords:
Flight dynamics
Free-molecular flow
Jet damping
Deep-space navigation

ABSTRACT

This paper contains the contents of the 20th John V. Breakwell Memorial Lecture delivered on October 1st, 2014, during the International Astronautical Congress in Toronto, Canada. The paper presents a few valuable and interesting lessons offered by unexpected dynamical performances of orbiting satellites. Sometimes, the observed dynamical behaviour appears to be 'anomalous', at least to an extent, when it does not conform to our a priori expectations. Subsequently, considerable effort is often required to properly understand that the observed behaviour is in fact perfectly natural from a dynamical point of view. The paper presents four examples from the author's background in the field of operational satellite flight dynamics. The first three events belong to the field of attitude dynamics of spin-stabilized satellites and the final case deals with the precise deep-space trajectory navigation of ESA's Rosetta satellite.

Contents

E-mail address: jvdha@aol.com

http://dx.doi.org/10.1016/j.actaastro.2015.04.020
0094-5765/

1. Introduction

John V. Breakwell (1917–1991)

This paper is dedicated to the memory of John V. Breakwell, whose ideas and enthusiasm inspired a generation of astrodynamicists. We are grateful to have had the good fortune to have known him [1–3].

The paper presents four examples of lessons learned from the in-orbit dynamical behaviour of satellites. The first three of these events belong to the field of attitude dynamics of spinning satellites and the last event deals with deep-space trajectory navigation.

The first event happened in May 1979 when ESA's spin-stabilized GEOS-1 satellite performed a 45-min orbit station-keeping manoeuvre [4]. Detailed simulations were carried out prior to the manoeuvre execution in order to verify the dynamical behaviour of the satellite's two flexible cable booms of 20-m lengths. Surprisingly, the simulation results predicted the complete de-spin within 10 min and, as a consequence, the loss of the satellite due to slackness of the cable booms. When examining these results with the help of dynamical models it became clear that the booms were *not* responsible for the mysterious de-spin. It was induced by the rate-coupling in the non-linear rigid-body Euler equations together with the relatively low spin rate of 11 rpm. Subsequently, two short trial manoeuvres were performed on the satellite, which confirmed that the predicted de-spin was real.

The second event happened on 18th December 1981, a few days after the launch of ESA's MARECS-A. During its geostationary transfer-orbit (GTO) phase, MARECS-A was spin-stabilized at a 65-rpm nominal spin rate. When checking the solar-aspect-angle measurements generated by the V-slit Sun sensor, unforeseen jumps in the Sun-aspect angle measurements of about 0.05° were observed around the three perigees [5]. No such jumps had been seen during previous ESA GTO's (e.g., GEOS and METEOSAT). Eventually, we confirmed [5,6] that these jumps were induced by free-molecular flow torques acting during the perigee passages.

The next event deals with NASA's CONTOUR satellite, which was lost during the firing of its solid rocket motor on 15th August 2002. This motor extended far into the satellite so that the lever arm of the jet-damping torque was relatively short. In addition, the variations in the satellite's mass properties during the rocket burn were relatively significant. Therefore, there was a suspicion that the anomaly could have been caused by stability issues during the burn. A representative practical jet-damping model was constructed [7]. This was based on the fundamental hypothesis that the angular momentum lost by the burning propellant must be equal to the momentum carried away by the combustion gases through the nozzle. Also, useful analytical models for the nutation induced by jet-damping and misalignment torques were established. Finally, it was confirmed [7] that the jet-damping torque was not responsible for the loss of CONTOUR.

The last event is relevant to planetary and comet-rendezvous missions, which require precise targeting based on the accurate non-gravitational modelling of the perturbing forces. Therefore, ESA uses high-fidelity models for the small forces induced by the solar radiation pressure acting on the satellite surfaces. Nevertheless, major discrepancies between the predicted and estimated forces were observed during the cruise phases of the Rosetta, Mars Express, and Venus Express satellites. Originally, these discrepancies were corrected by using scale factors for the acceleration components along the

satellite-sun direction. Our analyses [8–14] found that the anomalies originate from recoil forces induced by thermal radiation re-emitted from the satellite's exterior surfaces. These forces vary with the surface orientation and have in general non-zero components away from the Sun direction.

2. Satellite dynamics lesson

2.1. Background

When ESA's spin-stabilized GEOS-1 satellite (shown in Fig. 1) had to perform a 45-min north–south orbit station-keeping manoeuvre in May 1979 there was little ground for apprehension [4]. A similar (although much shorter) 3-min manoeuvre had performed smoothly two years earlier.

However, there were two apparent differences at this time. The two 20-m long radial cable booms had been deployed and the spin rate had been lowered from 96 to 11 rpm. Therefore, there was some concern about the dynamical behaviour of the cable booms during the manoeuvre. Simulations were carried out by means of the non-linear satellite dynamical model. Surprisingly, the results predicted a complete de-spin of the satellite (and loss of the satellite due to the slackness of the cable booms) after just 7.5 min from the start of the manoeuvre.

When analyzing the simulator results it became obvious that the booms were *not* responsible for the satellite's de-spin. In fact, the rate coupling in the non-linear rigid-body Euler equations together with the relatively low 11-rpm spin rate caused the potentially catastrophic spin-down.

Subsequently, two short verification manoeuvres were commanded to the satellite and the observed reductions in spin rates were consistent with the simulator's predictions. Boland and Janssens [4] provide a thorough first-hand narrative of this narrow-escape satellite saga.

The lesson in satellite dynamics recounted here captured the imagination of the author, who proceeded to develop an analytical higher-order perturbation model [15] for the attitude motion of a rigid-body satellite under a body-fixed torque. This model provides an independent confirmation of the observed GEOS-1 de-spin. Subsequently, it has also been used for the benefit of other satellites. For example, it was instrumental in establishing the most favourable configuration for the five mechanical gyros of the HIPPARCOS satellite. The objective was to maximize the overlaps in the two fields of view (which project onto the same focal plane of the on-board telescope) under reaction torques induced by the gyros [16]. Larger overlaps facilitated the subsequent star pattern recognition operations.

2.2. Dynamical model

For illustration, we present here an approximate method [4] for analyzing the attitude motion of an asymmetric spinning rigid body. The thrust force acts parallel to the spin axis as illustrated in Fig. 2. It generates a constant torque within the equatorial plane of the body reference frame.

The rotation rates governing the attitude motion obey the well-known Euler equations:

$$A\dot{\omega}_1+(C-B)\ \omega_2\,\omega_3=M_1$$

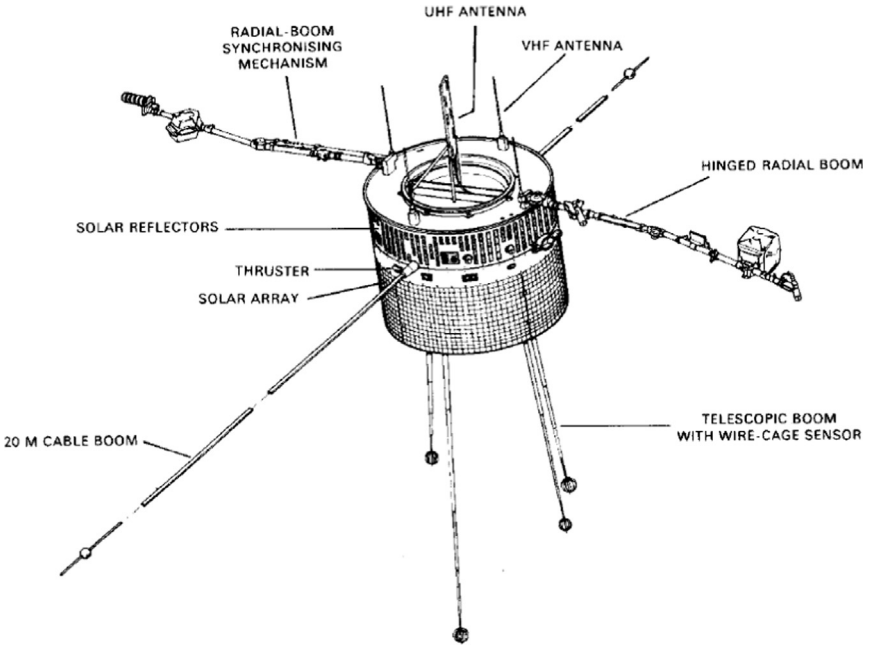

Fig. 1. In-orbit configuration of ESA's GEOS-1 satellite.

$$B\dot{\omega}_2-(C-A)\ \omega_1\ \omega_3=M_2$$
$$C\dot{\omega}_3+(B-A)\ \omega_1\ \omega_2=0 \qquad (1a\text{–}c)$$

The dots denote time-derivatives, ω_j are the components of the rotation vector $\boldsymbol{\omega}$ and the subscripts $j=1, 2, 3$ refer to the principal x, y, z body axes. The constants A, B, C are the principal moments of inertia with $A<B<C$. The axial force $\mathbf{F}$ and lever arm vector $\mathbf{r}$ (see Fig. 2) generate the torque $\mathbf{M}$ with components M_1 and M_2 along the x_1, x_2 body axes:

$$M_1=r\,F\ \sin\ \alpha; \qquad M_2=-r\,F\ \cos\ \alpha \qquad (2a,b)$$

We introduce now the inertia coefficients:

$$k_1=(C-B)/A\,; \qquad k_2=(C-A)/B; \qquad k_3=(B-A)/C \qquad (3a\text{–}c)$$

which satisfy $0<k_j<1$ ($j=1, 2, 3$). We write $m_j=M_j/I_j$ with units of $1/s^2$ and I_j denoting the moment of inertia about the x_j axis. This allows us to simplify the appearance of Eq. (1) as follows:

$$\dot{\omega}_1+k_1\ \omega_3\ \omega_2\ =m_1$$
$$\dot{\omega}_2-k_2\ \omega_3\ \omega_1\ =m_2$$
$$\dot{\omega}_3+k_3\ \omega_1\ \omega_2=0 \qquad (4a\text{–}c)$$

2.3. Approximate solutions for rates

Because GEOS-1 is a stable spinner the free-drift nutation remains small so we may assume that $\omega_j(0)\cong 0$ ($j=1, 2$). Eq. (4c) suggests that, at least initially, the change in spin rate $\omega_3(t)$ is also small:

$$w_3(t)\cong \mathrm{w}_3(0)=\Omega\ (\text{constant}) \qquad (5)$$

Eq. (4a,b) have now been linearized and have the periodic solutions:

$$\omega_1(t)\cong -a_2+a_2\ \cos(wt)+b_1\ \sin(wt)$$
$$\omega_2(t)\cong a_1-a_1\ \cos(wt)+b_2\ \sin(wt) \qquad (6a,b)$$

where w denotes the nutation rate:

$$w=\ \Omega\sqrt{k_1\ k_2} \qquad (7)$$

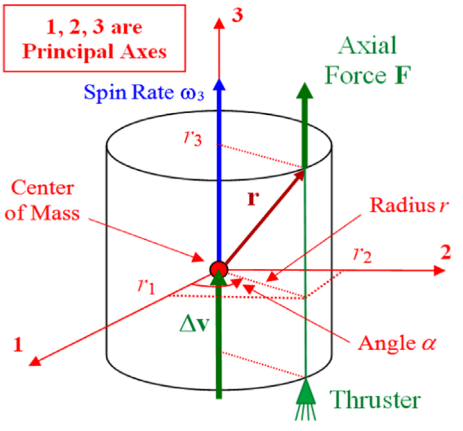

Fig. 2. Axial thruster executing $\Delta\mathbf{v}$ manoeuvre on a spin-stabilized satellite like GEOS-1.

and the constants a_j and b_j stand for:

$$a_j=m_j/(k_j\,\Omega); \qquad b_j=m_j/w \qquad (j=1,2) \qquad (8a,b)$$

In order to analyze the spin behaviour we substitute the periodic equatorial x, y rates of Eq. (6) into Eq. (4c). Since our focus is on the long-term evolution of the spin rate we replace the forcing term in Eq. (4c) by its average value over the nutation period $P_{nut}=2\pi/w$:

$$\dot{\omega}_3\approx -k_3\langle\omega_1(t)\,\omega_2(t)\rangle=-\frac{k_3}{P_{nut}}\int_0^{P_{nut}}\{\omega_1(s)\,\omega_2(s)\}\,ds=k_3\frac{m_1\,m_2}{w^2} \qquad (9)$$

From Eq. (2) we find that the result of Eq. (9) will be non-zero as long as $\alpha\neq 0$ and $\alpha\neq k\pi/2$ ($k=1, 2,\ldots$). In this case, the spin rate $\omega_3(t)$ will be varying with time. The definition of the *initial* nutation rate in Eq. (7) is based on the initial spin rate Ω. Subsequently, the definition of the *instantaneous* nutation rate in Eq. (7) should be based on $\omega_3(t)$ and will thus also be time-varying. After replacing w by the instantaneous nutation rate in Eq. (9) we obtain the following equation for the spin rate $\omega_3(t)$:

$$\dot{\omega}_3(t)\cong\frac{k_3\,m_1\,m_2}{k_1\,k_2\,\omega_3^2} \quad\Rightarrow\quad \left(\omega_3^3\right)^{\cdot}=3J\,M_1\,M_2 \qquad (10a,b)$$

with:

$$J=\frac{B-A}{C(C-B)\,(C-A)} \qquad (10c)$$

Since all terms on the right-hand-side of Eq. (10b) are constants we can easily integrate:

$$\omega_3(t)=\Omega\left(1+t/\tau\right)^{1/3} \qquad (11a)$$

Finally, the constant parameter τ can be expressed in the torque parameters defined in Eq. (2):

$$\tau=\Omega^3/\,(3J\,M_1\,M_2)=-\Omega^3/\left(3J\,r^2F^2\ \sin\ \alpha\ \cos\ \alpha\right) \qquad (11b)$$

This expression confirms that a spin-down occurs in the case when $0<\alpha<90^\circ$.

The input parameters for GEOS-1 are as follows [4]:

$$\left.\begin{array}{ll} F=7.0\ N; & r=0.725\ m; \quad \alpha=40^\circ \\ \Omega=11\ rpm; & J=\ 8.914\ \times 10^{-5}\ kg^{-2}m^{-4}\end{array}\right\}$$
$$\Rightarrow \quad \tau=451\ s \qquad (12a\text{–}f)$$

Ref. [4] shows how the contributions of the cable-booms to the inertias B and C should be included in the calculation of the parameter J.

Fig. 3 shows the spin rate variations for thrust durations of up to one hour and initial spin rates between 11 and 60 rpm. When using the GEOS-1 parameters we find that a complete de-spin of the satellite will happen within an hour for any initial spin rate that is below 22 rpm.

3. Free-molecular flow lesson

3.1. MARECS-A solar aspect angle measurements

The next example occurred during the geostationary transfer orbit (GTO) of ESA's MARECS-A satellite in December 1981 following its injection by an Ariane-1 launch

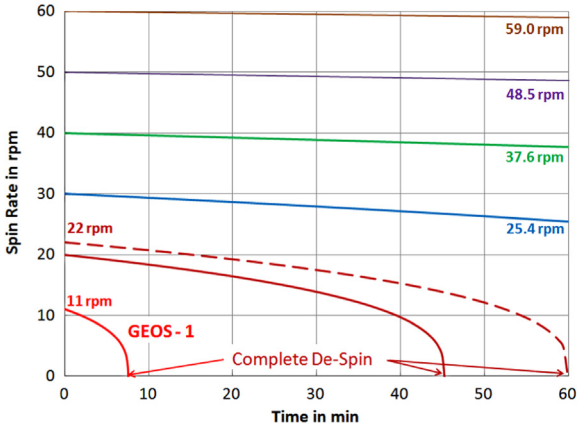

Fig. 3. Spin-rate variations under axial thrust for different initial spin rates.

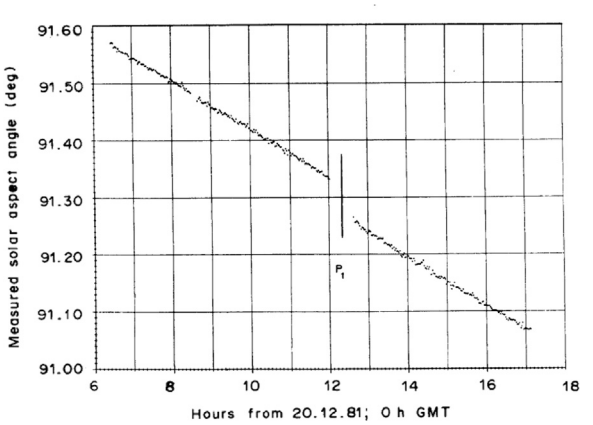

Fig. 4. Solar-aspect-angle measurements near MARECS-A 1st Perigee Passage (20.12.1981).

vehicle. MARECS-A was spin-stabilized with a spin rate of about 65 rpm during its GTO-phase.

When filtering the solar aspect angle outputs of the V-slit Sun sensor, unexpected discontinuities of about 0.05° were observed [5] in the evolution of the solar aspect angles around all of its three GTO perigees. Fig. 4 shows the measured solar aspect angles near the 1st perigee. It may be noted that no jumps had been observed during prior GTO's of ESA's GEOS and METEOSAT satellites.

A detailed study [5,6] reveals that the observed changes in the MARECS-A solar aspect angles are due to changes in the spin-axis attitude orientation over the perigee region. These attitude changes are induced by free-molecular flow (FMF) torques acting in the perigee region. GTO satellites launched by Ariane-1 have their perigees at close to 200 km altitude and FMF effects are appreciable during only about 20 min centred at the perigee.

The solar aspect angles represent the only available attitude-related measurements in the perigee region. It should be noted that V-slit Sun sensors can observe only a single component of the change in spin-axis orientation, namely the one normal to the Sun cone. (Note that a 'Sun cone' has its centreline in the Sun direction and represents the locus of attitude vectors with identical solar aspect angle.) If, in addition, the torque direction is known to good precision, it becomes feasible to calculate the total change in the spin-axis attitude from the observed jump in solar aspect angle.

In the case of MARECS-A the torque direction can be predicted by precisely modelling the free-molecular flow interactions with the applicable satellite surfaces. In this manner we found [5] that the FMF torque points in a direction that is about 11° away from the maximum possible change in Sun-angle. Since the spin-axis precession moves in the direction of the applied torque its direction in inertial space is known. On this basis we can calculate that the magnitude of the spin-axis attitude change is 1.87% larger than the observed jumps in solar aspect angles.

3.2. Background of free-molecular flow effects

In the early 1980s Koppenwallner [17] and co-workers [18] established numerical models for calculating the forces and torques generated by free-molecular flow effects on the basis of Maxwell–Boltzmann's kinetic gas theory. These models have been used for evaluating the FMF forces and torques acting on ESA satellites like MARECS-A [19]. Furthermore, wind tunnel tests were conducted [20] to reproduce the attitude changes of MARECS-A during its GTO perigee passages.

Around the same time, the author developed detailed analytical models [5,6] that predict the attitude changes induced by the free-molecular flow effects for cylindrical and box-shaped satellites in GTO. When allowing for typical uncertainties in the air densities, the analytical results confirm that the MARECS-A attitude changes are induced by FMF torques acting over the perigee region.

In the analytical model, the momentum interactions governing the torque's magnitude and direction are expressed as functions of the orbital eccentric anomaly. The cumulative torque vector over the perigee region is obtained by analytical integration with the help of an asymptotic method. This torque forces the spin-axis orientation precession in the direction normal to the plane formed by the perigee velocity and the spin-axis orientation vectors (with both vectors referring to the same inertial frame).

Of particular interest is the generic expression [5] for the FMF torque that is valid for a symmetrical satellite configuration, which incorporates the orbital velocity and satellite spin-axis vectors. Furthermore, it contains the environmental parameters such as the local air density and scale height, the FMF characteristics in terms of the diffuse and specular reflectivity parameters, the velocities of the incident and reflected molecules, as well as the satellite's geometrical configuration parameters.

Obviously, the forces and torques induced by FMF act predominantly within the perigee region. For a typical GTO, the 1% threshold level of the maximum perigee density is reached at the eccentric anomaly values of $E = \pm 7.5°$. Therefore, the forces and torques induced by the FMF are practically negligible beyond this 7 min long interval centred at the perigee. The exponential density model may thus be expanded in an asymptotic power series in terms of the eccentric anomaly.

Elliptical GTO's have relatively large values for the parameter $\beta = ae/H_p$, where a is the semi-major axis, e is the eccentricity, and H_p is the density scale height at perigee (for instance, $\beta \approx 539$ for MARECS-A). The spin-axis attitude change over the perigee region will be formulated in terms of a power series in the small parameter $1/\beta = H_p/(ae)$ and its geometrical interpretation will be evaluated.

3.3. Free-molecular force and torque models

3.3.1. Generic force model

The FMF provides the dominant perturbing force acting on Earth-orbiting spinning satellites below about 600 km altitude. The density within the Earth's thermosphere is mainly affected by temperature variations due to the absorption of extreme solar ultra-violet radiation. These processes can be monitored on Earth via the $F_{10.7}$ solar flux index.

Klinkrad and Fritsche [21] offer a generic aerodynamic force model that expresses the FMF force **F** acting on a flat satellite surface:

$$\mathbf{F} = \frac{1}{2}\rho A\, v_i^2\, \mathbf{C} \tag{13}$$

The local atmospheric density ρ follows by summing the concentration profiles of the atmospheric constituents (e.g., N_2, O_2, O, He, Ar, H, N). The parameter A refers to the applicable surface area in m^2. The free-stream molecular incident velocity v_i is practically identical to the negative orbital velocity $-v$. The non-dimensional vector parameter **C** is a function of the satellite's geometrical parameters, its orientation with respect to the flow, as well as the accommodation coefficients. In fact, **C** provides a concise representation of the familiar *drag* and *lift* coefficients.

The calculation of the aerodynamic forces requires the modelling of the intricate molecular interactions with the satellite surfaces that are exposed to the flow. This may be done as in Ref. [6] by introducing accommodation coefficients but here an alternative approach is followed. We assume that a fraction of the molecules is reflected *specularly*, i.e. an elastic reflection of the molecules with net momentum transfer in the surface-normal direction only. The remaining molecules are adsorbed on the surface and may experience collisions with the surface molecules before being re-emitted in an arbitrary direction, i.e. *diffusely*.

The net force resulting from the diffuse re-emission acts also normal to the surface. In this case, however, the momentum transfer generates an additional tangential force component (if the incidence direction is *not* normal to the surface) because of the adsorption of the incident molecules.

The relationship between the unit-vectors **u**, **n**, and **t** follows from the geometry shown in Fig. 5:

$$\mathbf{u} = \cos\vartheta\, \mathbf{n} + \sin\vartheta\, \mathbf{t} \tag{14}$$

The fraction of incident molecules that is reflected *diffusely* is denoted by σ_d ($0 \le \sigma_d \le 1$). We assume that the nature of the re-emission will be in accordance with Lambert's cosine law as shown in Fig. 5. These molecules lose almost all of their momentum since they become accommodated on the surface. Subsequently, they are emitted diffusely with the most probable velocity v_w predicted by Maxwell–Boltzmann's velocity distribution associated with the surface temperature T_w. The recoil force due to the re-emission acts *normal* to the surface in the direction of its (inward) normal vector **n**.

The non-diffusely reflected fraction $(1-\sigma_d)$ of the molecules is reflected specularly. These molecules are *not* accommodated on the surface and preserve their incoming tangential velocity components without any momentum exchange in the tangential direction.

The velocity components normal to the surface change their signs during the reflection off the surface. They produce a recoil force (in the normal direction) of the same magnitude as the force that was generated by the incident molecules. Thus, the coefficient **C** in Eq. (13) may be split up in diffuse and specular parts:

$$\mathbf{C} = \sigma_d \mathbf{c}_d + \sigma_s \mathbf{c}_s; \quad with: \quad \sigma_s = 1 - \sigma_d \tag{15}$$

where the coefficients $\mathbf{c}_d$ and $\mathbf{c}_s$ represent the diffuse and specular momentum interactions with the surface A, respectively.

Practical free-molecular force models can be derived from Maxwell–Boltzmann's kinetic theory of gases, see Koppenwallner [17]. This involves the use of the *pressure* and *particle flux* functions Π and χ. The results for the coefficients $\mathbf{c}_d$ and $\mathbf{c}_s$ may then be expressed in the surface (or wall) temperature T_w and atmospheric molecular temperature T_m as follows:

$$\mathbf{c}_d = \left(\frac{v_m}{v_i}\right)^2 \left\{ \left(\frac{\Pi(S_n)}{\sqrt{\pi}} + \frac{1}{2}\sqrt{\frac{T_w}{T_m}}\chi(S_n) \right)\mathbf{n} + \left(\frac{S_t \chi(S_n)}{\sqrt{\pi}} \right)\mathbf{t} \right\} \tag{16a}$$

$$\mathbf{c}_s = \frac{2}{\sqrt{\pi}}\left(\frac{v_m}{v_i}\right)^2 \Pi(S_n)\mathbf{n} \tag{16b}$$

with subscripts m=molecular, i=incident, n=normal, t=tangential, w=wall, and abbreviations:

$$\Pi(S_n) = S_n \exp(-S_n^2) + \sqrt{\pi}\left(S_n^2 + 0.5\right)\{1 + erf(S_n)\} \tag{17a}$$

$$\chi(S_n) = \exp(-S_n^2) + \sqrt{\pi}\, S_n \{1 + erf(S_n)\} \tag{17b}$$

$$S_n = (v_i/v_m)\cos\vartheta; \quad S_t = (v_i/v_m)\sin\vartheta; \tag{17c–d}$$

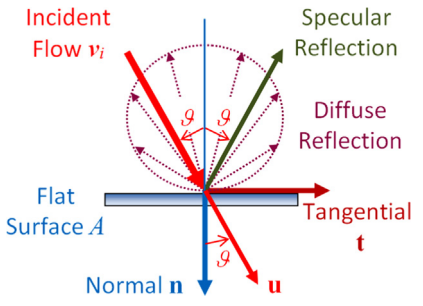

Fig. 5. Illustration of diffuse and specular reflections and definitions of unit-vectors **u**, **n**, **t**.

$$\sqrt{(T_w/T_m)} = v_w/v_m \tag{17e}$$

3.3.2. Simplified aerodynamic coefficients

When S_n is sufficiently large, Eq. (17a,b) may be simplified (with errors $< 10^{-6}$ for $S_n > 3.5$):

$$\Pi(S_n) \cong \sqrt{\pi}\left(2S_n^2+1\right); \quad \chi(S_n) \cong 2\sqrt{\pi}\, S_n \tag{18a, b}$$

Although the velocity ratio $v_i/v_m > 5$ for altitudes above 150 km, the validity of the approximate results in Eq. (18) breaks down when $\vartheta \cong 90^\circ$. Fortunately, the surface incidence angle is shallow in this case so that the force is relatively small and the resulting errors will be immaterial.

The expressions in Eq. (18) enable us to simplify Eq. (16) as:

$$\mathbf{c}_d \cong \left[2\cos^2\vartheta + \left(\frac{v_m}{v_i}\right)^2 + \sqrt{\pi}\left(\frac{v_w}{v_i}\right)\cos\vartheta\right]\mathbf{n} + \sin(2\vartheta)\,\mathbf{t} \tag{19a}$$

$$\mathbf{c}_s \cong 2\left[2\cos^2\vartheta + \left(\frac{v_m}{v_i}\right)^2\right]\mathbf{n} \tag{19b}$$

The aerodynamic coefficient $\mathbf{C}$ in Eq. (15) becomes now:

$$\mathbf{C} = \left\{(2-\sigma_d)\left[2\cos^2\vartheta + \left(\frac{v_m}{v_i}\right)^2\right] + \sigma_d\sqrt{\pi}\left(\frac{v_w}{v_i}\right)\cos\vartheta\right\}\mathbf{n} + \sigma_d \sin(2\vartheta)\,\mathbf{t} \tag{20a}$$

$$\Rightarrow \quad \mathbf{C} = C_n\,\mathbf{n} + C_t\,\mathbf{t} \tag{20b}$$

where the scalar FMF parameters C_n, C_t are defined by:

$$C_n = c_0 + c_1\cos\vartheta + c_2\cos^2\vartheta; \quad C_t = \sigma_d \sin(2\vartheta) \tag{21a, b}$$

and:

$$c_0 = (2-\sigma_d)\left(\frac{v_m}{v_i}\right)^2; \quad c_1 = \sigma_d\sqrt{\pi}\left(\frac{v_w}{v_i}\right); \quad c_2 = 2(2-\sigma_d) \tag{22a–c}$$

These coefficients may be interpreted physically as follows: c_0 models the normal momentum transfer due to the thermal speeds of the incident and specularly reflected molecules; c_1 refers to the normal momentum transfer of molecules that are diffusely re-emitted at surface temperature (after accommodation); c_2 denotes the normal momentum transfer due to the velocities of the incident and specularly reflected molecules. Finally, the parameter C_t expresses the transfer of tangential momentum by the incident molecules that are accommodated on the surface.

Fig. 6 shows the FMF coefficients C_n and C_t as functions of ϑ for σ_d in the range from 0.9 to 1.0. Note that $\sigma_d > 0.95$ at about 200 km [22]. Additional inputs are $T_w/T_m \cong 0.3$ and $v_i/v_m \cong 10$. The results of C_n and C_t for $\sigma_d = 0.9$ are at most 10% different from those for $\sigma_d = 1$. These results hardly change for different v_m/v_i ratios because the parameter c_0 in Eq. (22a) is comparatively small since $c_2 \cong 25c_1$ and $c_1 \cong 8c_0$.

The *drag* and *lift* coefficients C_D and C_L follow from Eqs. (20)–(22), see also Fig. 5:

$$\begin{pmatrix} C_D \\ C_L \end{pmatrix} = \begin{bmatrix} \cos\vartheta & \sin\vartheta \\ -\sin\vartheta & \cos\vartheta \end{bmatrix} \begin{pmatrix} C_n \\ C_t \end{pmatrix} \tag{23}$$

The magnitude of C_L is typically less than 10% of C_D.

It follows from Eqs. (13) and (20) that the components of the FMF force along the normal and tangential directions (see Fig. 5) may be written as:

$$\mathbf{F} = \frac{1}{2}\rho\, v^2 A\,(C_n\,\mathbf{n} + C_t\,\mathbf{t}) \tag{24}$$

where v is the satellite's orbital velocity, which may be taken identical to $-v_i$. The coefficients C_n and C_t are defined in Eq. (21) and the unit-vectors $\mathbf{n}$ and $\mathbf{t}$ refer to the geometry of Fig. 5. Eq. (24) is consistent with Ref. [6], Eq. (28), which was derived by using accommodation coefficients.

3.3.3. Integrated torque result

Reference [23] presents the detailed derivation of the integrated torque expressions for box-shaped as well as cylindrical satellite configurations. These represent the FMF torques contributed by the satellite top and side surfaces after averaging over a spin period.

The generic result for the spin-averaged FMF torque of cylindrical and box-shaped satellite configurations is given by:

$$\langle\mathbf{M}\rangle = -\frac{1}{2}\rho\,(\mathbf{z}\times\mathbf{v})\{C_0 v^2/|\mathbf{z}\times\mathbf{v}| + C_1 v + C_2|\mathbf{z}\times\mathbf{v}| + C_3(\mathbf{z}\bullet\mathbf{v})\} \tag{25}$$

Table 1 provides the parameters C_j for a box-shaped satellite like MARECS-A and Fig. 7 defines the geometrical parameters used in Table 1.

3.4. Calculation of change in spin-axis orientation

3.4.1. Orbit model

The satellite's velocity vector is expressed in terms of the eccentric anomaly E. Its components in the perigee reference frame (see Fig. 8) with vertical and horizontal

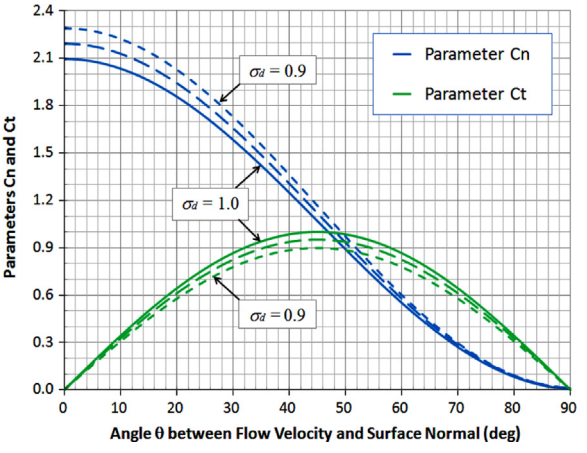

Fig. 6. FMF parameters C_n and C_t as functions of ϑ.

unit vectors ξ_p,η_p are:

$$\mathbf{v}(E)=\sqrt{\mu/a}\{-(\sin E)\,\xi_p+s_e(\cos E)\,\eta_p\}/(1-e\cos E) \tag{26}$$

where a is the semi-major axis, e is the eccentricity, $s_e=\sqrt{(1-e^2)}$, and $\mu=3.986\times10^{14}$ m^3/s^2 is the Earth's gravitational parameter. The magnitude of the velocity vector is given by:

$$v(E)=\sqrt{(\mu/a)\,\{(1+e\cos E)/(1-e\cos E)\}} \tag{27}$$

The atmospheric density is adopted from King-Hele's exponential model [24]:

$$\rho(E)=\rho_p\exp\{-\beta(1-\cos E)\} \tag{28}$$

Here, ρ_p denotes the atmospheric density at the perigee position r_p and the parameter β is defined by:

$$\beta=ae/H_p \tag{29}$$

with H_p the density scale height at perigee.

For the MARECS-A GTO parameters of $a\cong2.44\times10^4$ km, $e\cong0.73$, $H_p\cong33$ km we find $\beta\cong539$. The density decreases rapidly from its maximum value ρ_p at perigee. The threshold density level of 1% of ρ_p occurs at $E=\pm7.5^\circ$, which corresponds to an interval of only ±3.6 min. Therefore, we may neglect torque contributions beyond this relatively narrow range of eccentric anomaly.

3.4.2. Change in spin-axis angular momentum

First, we transform the starting spin-axis vector from its inertial representation $\mathbf{z}=(z_1, z_2, z_3)^T$ to its coordinates $(z_\xi, z_\eta, z_\zeta)^T$ in the perigee reference frame of Fig. 8:

$$\mathbf{z}=z_\xi\,\xi_p+z_\eta\eta_p+z_\zeta\,\xi_p \tag{30a}$$

with cone and clock angles λ_p, μ_p:

$$z_\xi=\sin\lambda_p\cos\mu_p;\quad z_\eta=\cos\lambda_p;\quad z_\zeta=\sin\lambda_p\sin\mu_p \tag{30b}$$

The spin-averaged torque vector of Eq. (25) can be expressed in the eccentric anomaly by substituting the velocity and attitude results of Eqs. (26) and (30):

$$\langle\mathbf{M}(E)\rangle=-\frac{1}{2}\rho_p\left(\frac{\mu}{a}\right)\frac{F(E)}{(1-e\cos E)^2}\{s_e\cos E\,(\mathbf{z}\times\eta_p)-\sin E\,(\mathbf{z}\times\xi_p)\}\exp[-\beta(1-\cos E)] \tag{31}$$

where $F(E)$ is defined by Eq. (18) of Ref. [5].

The change $\Delta\mathbf{H}$ in the satellite's angular momentum vector $\mathbf{H}=I_z\,\boldsymbol{\omega}_{spin}$ (where I_z is the axial moment of inertia) follows by integration of Eq. (31) over the perigee region:

$$\Delta H=\int_{t_p-t_1}^{t_p+t_1}\langle\mathbf{M}(t)\rangle\,dt$$

Table 1
Parameters C_j (j=0,…, 3) for a box-shaped satellite.

Parameters in m^3	Box-shaped satellite
C_0	$2(A_1+A_2)R_z\,c_0/\pi$
C_1	$R_z(A_1+A_2)\,c_1/2$
C_2	$4R_z(A_1+A_2)(C_2+\sigma d)/(3\pi)$
C_3	$(2A_0\,R_0-A_1\,R_x-A_2\,R_y)\,\sigma_d$

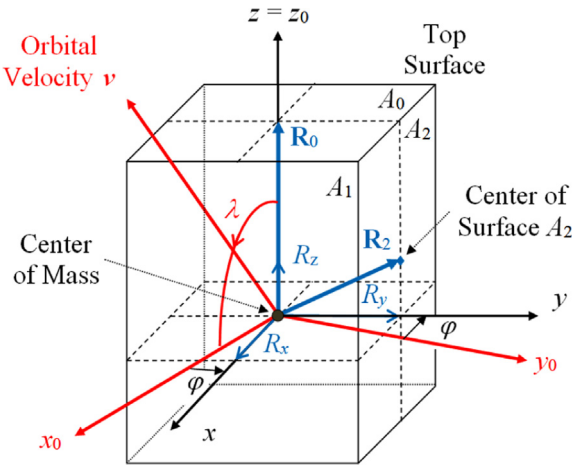

Fig. 7. Definition of reference axes and parameters.

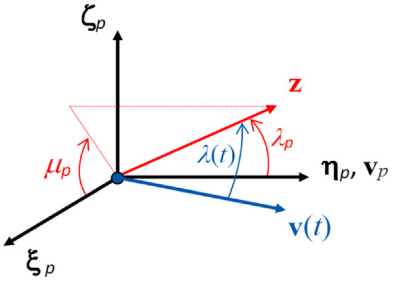

Fig. 8. Definitions of cone and clock angles λ_p, μ_p.

$$=\sqrt{(a^3/\mu)}\int_{-E_1}^{+E_1}\langle\mathbf{M}(E)\rangle\,(1-e\cos E)\,dE \tag{32}$$

Since the integration interval is taken symmetric about the perigee position E=0, odd functions of E do not contribute to the integral in Eq. (32) so we write:

$$\Delta H=-\rho_p\sqrt{\mu a}\{(\mathbf{z}\times\eta_p)J_1(E_1)-(\mathbf{z}\times\xi_p)J_2(E_1)\} \tag{33}$$

The integrals J_m (E_1), m=1, 2 are defined by:

$$J_m(E_1)=\int_{-E_1}^{E_1}G_m(E)\,\exp[-\beta(1-\cos E)]\,dE \tag{34}$$

where the functions $G_m(E)$ have units of m^3 and denote the surviving even terms in the integrand of Eq. (32), which are given in explicit forms in Eq. (25) of Ref. [5].

The integrals in Eq. (34) can be simplified by using the integration variable $u=\sqrt{(1-\cos E)}$ and by expanding $G_m\{E(u)\}$ in power series of u. Since the parameter β is large, the exponential term in Eq. (34) obtains its major contributions from a small region around the perigee. Application of the Laplace Method [5] with variable u and parameter β leads to a compact asymptotic result for $\Delta\mathbf{H}$ in Eq. (33):

$$\Delta H\cong-\rho_p\sqrt{\frac{2\pi\mu a}{\beta}}\{\gamma_{10}(\mathbf{z}\times\eta_p)$$

$$+\frac{1}{2\beta}[\gamma_{11}(\mathbf{z}\times\boldsymbol{\eta}_p)-\gamma_{21}(\mathbf{z}\times\boldsymbol{\xi}_p)]+O\left(\frac{1}{\beta^2}\right)\Big\} \tag{35}$$

The indices (i.e., $m=1, 2$; $k=0, 1$) of the coefficients γ_{mk} refer to the functions $G_m[E(u)]$ and to the power of the asymptotic power series in $(1/\beta)^{k+1/2}$, respectively. The coefficients for $k=0$ are the leading terms of the asymptotic expansion in Eq. (35). The γ_{20} term vanishes and γ_{10} is defined by:

$$\gamma_{10}=(1+e)\{C_0/\ \sin\ \lambda_p+C_1+C_2\ \sin\ \lambda_p+C_3\ z_\eta\} \tag{36}$$

The second term in Eq. (35) (i.e., the one containing […]) is of the order of $(1/\beta)^{3/2}$ so that its magnitude is only about 0.2% of the leading γ_{10} term for typical GTO conditions. Thus, we may neglect the second term so that only the γ_{10} term of Eq. (35) needs to be taken into account.

3.4.3. Change in spin-axis attitude

The coordinates of the spin-axis vector $\mathbf{z}^+$ (i.e., *after* perigee) in the perigee reference frame follow from $\boldsymbol{\Delta H}$ in Eq. (35) (when assuming that any nutation disturbances have subsided):

$$\mathbf{z}^+=\mathbf{z}+\boldsymbol{\Delta z}\cong(z_\xi+\varepsilon\, z_\zeta)\boldsymbol{\xi}_p+z_\eta\boldsymbol{\eta}_p+(z_\zeta-\varepsilon\, z_\xi)\boldsymbol{\zeta}_p \tag{37a}$$

$$\Rightarrow\qquad \boldsymbol{\Delta z}\cong\varepsilon\ \sin\ \lambda_p(\sin\ \mu_p\ \boldsymbol{\xi}_p-\ \cos\ \mu_p\ \boldsymbol{\zeta}_p) \tag{37b}$$

with:

$$\varepsilon=\frac{\Delta H}{H}\cong\gamma_{10}\,\rho_p\frac{1}{H}\sqrt{\frac{2\pi\mu a}{\beta}}\qquad [rad] \tag{38}$$

The magnitude of the attitude change follows from Eq. (37b):

$$|\boldsymbol{\Delta z}|\ \cong\ \varepsilon|\boldsymbol{\eta}_p\times\mathbf{z}\,|\ \cong\varepsilon\ \sin\ \lambda_p \tag{39}$$

As expected, the angle λ_p between the velocity vector at perigee and the original spin-axis attitude plays a significant role in the present analysis.

Because of the dominance of the torque vector in the perigee region, the vectors $\boldsymbol{\Delta H}$ and $\boldsymbol{\Delta z}$ point along the direction $\boldsymbol{\eta}_p\times\mathbf{z}$ as indicated by the leading term in Eq. (35). Thus, the spin axis $\mathbf{z}$ rotates along the cone centred about the $\boldsymbol{\eta}_p$ axis with cone angle λ_p, see Fig. 8. The change in spin-axis orientation has the magnitude of $\varepsilon\ \sin\lambda_p$ as predicted by Eq. (39).

3.5. Discussion of results

Simulations have been performed on the basis of MARECS-A geometrical configuration, its spin-axis attitude orientation, and its GTO orbital characteristics [23] to identify the influences of each of the various input variables. Fig. 9a shows the FMF torque (normalized by $\rho\ v^2$) as function of the angle λ_p. The MARECS-A input value $\lambda_p=17.4^\circ$ is highlighted in Fig. 9.

Fig. 10 shows the variations in the spin-axis attitude changes under different atmospheric density levels (i.e., maximum, mean, and minimum conditions) on the basis of the MSIS empirical model [25]. These results indicate that the spin-axis attitude changes resulting from this range of density levels varies by a factor of about 3. It should be noted that the observed attitude changes of about 0.05° for MARECS-A are just above the maximum density levels predicted by the MSIS model.

4. Jet damping lesson

4.1. CONTOUR solid rocket motor firing

CONTOUR (Comet Nucleus Tour) was a mission in NASA's Discovery Program aiming at imaging and science investigations of comet nuclei. Its main targets were the comets Encke, Schwassmann-Wachmann-3, and d'Arrest. CONTOUR was launched on July 3, 2002, by a Delta-7425 Launcher and injected into an Earth-phasing orbit of 1.75-day period. During the 6 weeks in these orbits, it was kept spin-stabilized at nominal spin rates of 20 and 60 rpm. A large number of orbit and attitude manoeuvres [26,27] were performed in order to achieve the most favourable conditions prior to the trajectory injection. CONTOUR's performance during these phasing orbits was flawless.

On 15th August 2002, CONTOUR was injected into its heliocentric trajectory to Encke's comet by a STAR-30BP Solid Rocket Motor (SRM). However, a mishap occurred near the end of the SRM burn and contact could not be re-established. Farquhar [28] conveys a detailed first-hand narrative of this unfortunate satellite saga.

Initially, the jet-damping effect was considered to be one of the most likely potential causes for the failure. CONTOUR's SRM extends far into the satellite so that the lever arm of the jet-damping torque is relatively short. Furthermore, the relatively large variations in the system mass properties during the burn raised the concerns about the attitude pointing stability.

Reference [7] presents the analyses and results of a detailed investigation evaluating the possibility of an instability induced by the jet-damping and misalignment torques. It examines the dynamical processes occurring within a spinning satellite during the SRM burn.

The equations of motion are derived for a system consisting of the rigid-body satellite plus the gases in the SRM combustion chamber *without* presuming a specific gas-flow model. Instead, Ref. [7] uses the fundamental conservation of the angular momentum from the SRM's solid propellant to the combustion gases leaving the system through the SRM

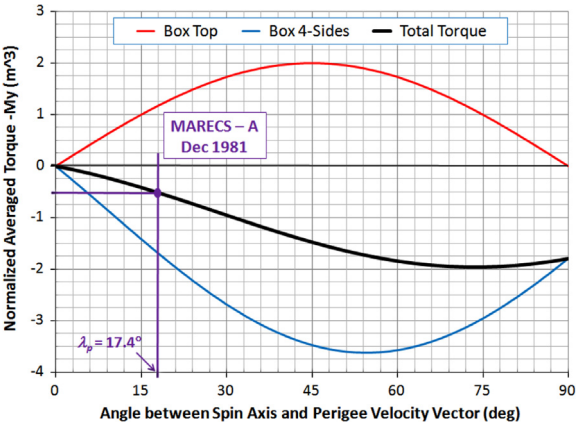

Fig. 9. Normalized torque on a box-shaped satellite.

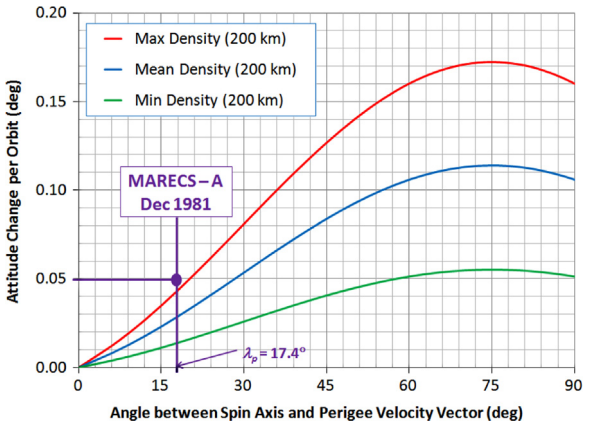

Fig. 10. Attitude changes for different density levels.

nozzle. Thus, the angular momentum flux from the diminishing inertia of the solid propellant is taken equal to the angular momentum flux of the gases exiting the nozzle.

The formal derivation [7] uses the theory of a variable-mass system and arrives naturally at expressions for the jet-damping and the SRM-thrust misalignment torques. The formulation employs the mass-flow centre $\boldsymbol{\rho}_\mathbf{e}$ and the mean exhaust velocity $\mathbf{v}_\mathbf{e}$. These two variables incorporate the action of the gases on the system independently of the flow model. Compact analytical results are derived for the torque effects on the attitude motion. Piecewise linear approximations are introduced for modelling the evolutions of the system mass properties during the burn. This flexible approach is well suited for a realistic description of the time-varying system parameters. The application of the proposed model will be illustrated for the specific CONTOUR conditions during its SRM burn.

4.2. Jet damping and misalignment torques

The main causes affecting the pointing stability of a spin-stabilized satellite during an SRM burn are misalignment and jet-damping torques. The misalignment torque is caused by offsets in the direction of the SRM thrust and in the location of the satellite's centre-of-mass due to imperfections in the satellite balancing and alignments. The jet-damping torque originates from the resistance of the out-flowing SRM gases against a transverse rotation.

Fig. 11 shows the (x, y, z) reference fame, which is fixed to the rigid part of the satellite and rotates with the instantaneous rotation vector $\boldsymbol{\omega}$. Reference [7] gives the detailed derivation of the equations of motion under misalignment and jet damping torques starting from the well-established moment equation for a non-inertial variable-mass system. After a substantial effort, the final form for the Euler equations under the apparent Coriolis and relative torques can be established as:

$$I\,\dot{\boldsymbol{\omega}} + \boldsymbol{\omega} \times \mathbf{H} + \beta\{\boldsymbol{\rho}_\mathbf{e} \times (\boldsymbol{\omega} \times \boldsymbol{\rho}_\mathbf{e})\} + \beta(\boldsymbol{\rho}_\mathbf{e} \times \mathbf{v}_\mathbf{e}) = \mathbf{0} \tag{40}$$

This expression describes the satellite's rotational motion under the effects of the SRM gases represented by the vectors $\boldsymbol{\rho}_\mathbf{e}$ and $\mathbf{v}_\mathbf{e}$ as illustrated in Fig. 12. If we can solve the complex gas flow dynamics (coupled to the motion of the rigid part) to produce the precise evolutions of $\boldsymbol{\rho}_\mathbf{e}$ and $\mathbf{v}_\mathbf{e}$ as functions of time throughout the burn, Eq. (40) describes the corresponding exact evolution of the attitude motion.

For simplicity, we consider a *steady* flow field so that both $\boldsymbol{\rho}_\mathbf{e}$ and $\mathbf{v}_\mathbf{e}$ remain *constant* during the burn. The corresponding approximate solution for the attitude motion follows from the compact vector Eq. (40). This equation will be expressed in its components along the system's principal axes by expanding the jet-damping term $\boldsymbol{\rho}_\mathbf{e} \times (\boldsymbol{\omega} \times \boldsymbol{\rho}_\mathbf{e})$ and misalignment term $\boldsymbol{\rho}_\mathbf{e} \times \beta\,\mathbf{v}_\mathbf{e} \cong \boldsymbol{\rho}_\mathbf{e} \times (-\mathbf{F}_{\text{thrust}}) = -\mathbf{T}_{\text{thrust}}$ (where β denotes the mass flow parameter $-dm/dt$):

$$\begin{aligned} &I_x\,\dot{\omega}_x + (I_z - I_y)\;\omega_y\omega_z + \beta\ell^2\omega_x = T_{x,thrust} \\ &I_y\,\dot{\omega}_y - (I_z - I_x)\;\omega_x\omega_z + \beta\ell^2\omega_y = T_{y,thrust} \\ &I_z\,\dot{\omega}_z + (I_y - I_x)\;\omega_x\omega_y = T_{z,thrust} \end{aligned} \tag{41a–c}$$

Here, $\ell = |\boldsymbol{\rho}_\mathbf{e}|$ is the effective lever arm of the jet-damping torque shown in Fig. 12. Both the misalignment and jet damping torque components are taken to be constants here. This approximation can be considered realistic over short intervals of up to a few seconds during the burn.

Eq. (41) is valid within the body's principal reference frame. In reality, the thrust vector (which is aligned with $\mathbf{v}_\mathbf{e}$) may not coincide with the principal z-axis because of inertia imbalance effects. Furthermore, there may be deviations in the thrust direction caused by imperfections within the SRM and/or due to mounting misalignments with respect to the satellite centreline. Finally, the lever arm $\boldsymbol{\rho}_\mathbf{e}$ may not be aligned in the nominal direction due to offsets in the effective thrust vector relative to the system's centre of mass as illustrated in Fig. 13.

The pointing error of the SRM thrust vector $\mathbf{F}_{thrust}$ in the system principal reference frame will be modelled by the half-cone angle δ and the constant but unknown phase angle β in Fig. 13. The components of the *actual* thrust vector within the principal frame are thus:

$$\mathbf{F}_{thrust} = F_{thrust}(\sin\delta\,\cos\beta, \sin\delta\,\sin\beta,\;\cos\delta)^T \tag{42}$$

The pointing error δ consists of several independent error sources, including a SRM-internal thrust direction

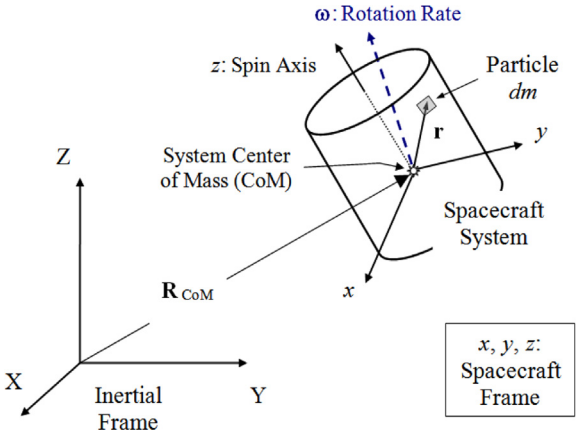

Fig. 11. Inertial and satellite reference frames.

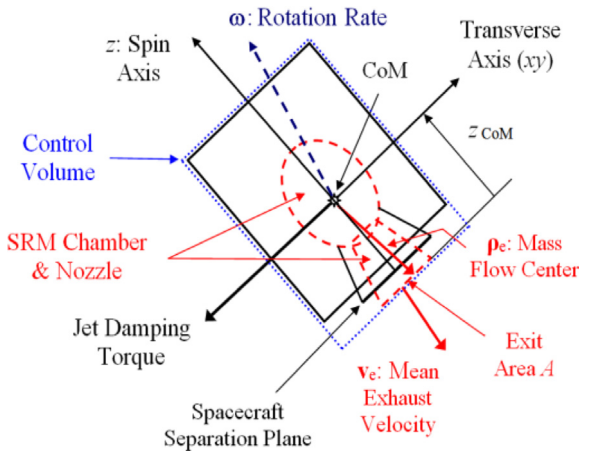

Fig. 12. Configuration and dynamical properties.

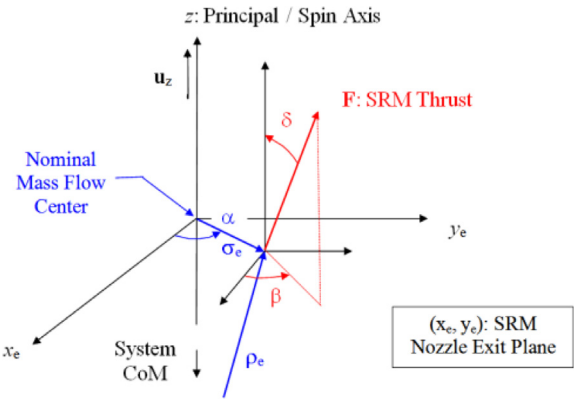

Fig. 13. SRM thrust vector in principal frame.

error, SRM mechanical misalignments, and satellite imbalance effects. The standard deviation of the angle δ is of the order of 0.1° and its phase angle β is uniformly distributed over the interval (0, 360°) in CONTOUR's case.

The magnitude of the SRM misalignment torque depends also on the position of the mass-flow centre $\boldsymbol{\rho_e}$ which points to the SRM nozzle exit plane as shown in Fig. 12. Ideally, this vector would be directed along the principal z-axis. In reality, however, the vector $\boldsymbol{\rho_e}$ may be misaligned in a direction normal to the z-axis so we have $\boldsymbol{\rho_e}=\ell\,\mathbf{u}_z+\boldsymbol{\sigma_e}$ as illustrated in Fig. 13. The vector $\boldsymbol{\sigma}_e$ refers to the small offset of the centre of the mass flow (x_e, y_e) within the nozzle exit plane. The standard deviation of CONTOUR's offset $\varepsilon=|\boldsymbol{\sigma_e}|$ is of the order of 1 mm and its phase angle α is uniformly distributed.

When expanding the force result in Eq. (42) for small values of δ and the vector $\boldsymbol{\rho_e}$ for small values of ε we obtain the following approximate expression for the misalignment torque:

$$\mathbf{T}_{thrust}=\boldsymbol{\rho_e}\times\mathbf{F}_{thrust}\cong F_{thrust}(\rho_x,\rho_y,\rho_z)^T \tag{43}$$

where:

$$\rho_x\cong\varepsilon\,\sin\,\alpha-\delta\ell\,\sin\,\beta;\qquad \rho_y\cong\delta\ell\,\cos\,\beta-\varepsilon\,\cos\,\alpha;$$
$$\rho_z\cong\varepsilon\delta\,\sin\,(\beta-\alpha) \tag{44}$$

The magnitude of the spin component of the misalignment torque is of second-order smallness. Its expected value is 0 with standard deviation $\frac{1}{2}\sqrt{2}\varepsilon\delta F_{thrust}$ Nm. Therefore, the effect of this torque component on the spin rate can be considered negligible in practice. In the special case of an axi-symmetric satellite we find from Eq. (41c) that $\omega_z(t)=\Omega$ (constant) throughout the SRM burn. For information, we mention that CONTOUR's input parameters predict a spin change of less than 0.1 rpm at the conclusion of the burn.

4.3. Rotational motion under disturbance torques

4.3.1. Solution for rates under jet-damping torque

Here we focus on the effect of the jet-damping torque. For simplicity, we consider an equivalent axi-symmetric satellite with $I=(I_x+I_y)/2$ at all times. A perturbation analysis shows that the qualitative behaviour of the results remains valid also for a small asymmetry in the moments of inertia.

We introduce the complex planar rotation rate $\boldsymbol{w}=\omega_x+j\omega_y$ (with j the imaginary unit) and combine Eqs. (41a,b):

$$\dot{\boldsymbol{w}}+\{d(t)-j\Omega\,n(t)\}\,\boldsymbol{w}=\mathbf{0} \tag{45}$$

with:

$$d(t)=\beta(t)\ell^2/I(t);\qquad n(t)=I_z(t)/I(t)-1 \tag{46a, b}$$

where $d(t)$ and $n(t)$ denote the jet-damping and nutation-frequency parameters, respectively, which account for the variations in the mass properties. Both parameters will be positive for a spin about the maximum principal axis.

The general solution of Eq. (45) is given by:

$$\boldsymbol{w}(t)=\boldsymbol{w}_0\,\exp\{-D(t)\}\exp\{j\,\Omega\,N(t)\} \tag{47}$$

with the positive functions $D(t)$ and $N(t)$ defined by:

$$D(t)=\int_0^t d(s)\,ds;\qquad N(t)=\int_0^t n(s)\,ds \tag{48a, b}$$

Eq. (47) contains two distinct effects. First, we have the decrease in nutation angle induced by the jet-damping torque and modelled by $\exp\{-D(t)\}$. Secondly, there is the variation of the nutation frequency due to the time-varying inertias and represented by $\exp\{j\Omega N(t)\}$.

4.3.2. Models for mass properties

The mass properties during the SRM burn vary as functions of time in a complex and poorly known manner. Consequently, there may be discrepancies of up to a few per cent between the predicted and actual in-orbit inertias. Therefore, linear models for the system mass properties may well be adequate. If more precise knowledge of the evolution of the mass properties over the burn is available the linear models presented here may be used with piecewise different parameters over each successive interval.

The instantaneous mass of the satellite-SRM system varies considerably during the SRM burn and will be modelled as a (piecewise) linear function of time:

$$m(t)=m_0-\beta\;t \tag{49}$$

where m_0 is the initial satellite-SRM mass and $\beta=-dm/dt$ is the (positive) mass flow parameter. For simplicity, β is kept

constant throughout the SRM burn. Again, if a more realistic mass-flow model is available, we may use a piecewise linear approach for better precision.

The moments of inertia decrease during the burn and are expressed by the linear models:

$$I(t) = I_0(1-\alpha\ t); \qquad I_z(t) = I_{z0}(1-\gamma\ t) \tag{50a, b}$$

where the coefficients α and γ represent the rates of decrease of the moments of inertia in units of s^{-1}.

The jet-damping function $d(t)$ and the nutation-frequency function $n(t)$ of Eq. (46) become now:

$$d(t) = d_0/(1-\alpha\ t) \tag{51}$$

$$n(t) = n_0\{1+(\alpha-\gamma I_{z0}/I_0)\ t\}\ /(1-\alpha\ t) \tag{52}$$

where d_0 equals $d(0)$ and $n_0 = I_{z0}/I_0 - 1$ is the ratio of the nutation and spin rates at the start of the burn.

After substituting these models for $d(t)$ and $n(t)$ into Eq. (48) and integrating over time, we obtain:

$$D(t) = -p\ \ell n\ [1-\alpha\ t] \tag{53}$$

$$N(t) = n_0 t - E\{t+(1/\alpha)\ \ell n\ [1-\alpha\ t]\} \tag{54}$$

with the dimensionless parameters p and E defined by:

$$p = d_0/\alpha\ ; \qquad E = (I_{z0}/I_0)(1-\gamma/\alpha) \tag{55a, b}$$

The ratio of the instantaneous nutation frequency to the spin frequency for a variable-mass system must account for the continuously varying mass properties and is defined as (see Janssens [29], Eq. 9):

$$\frac{N(t)}{t} = \left\{\Omega \int_0^t n(s)\ ds\right\}\frac{1}{\Omega\ t} = n_0 - E - \frac{E}{\alpha\ t}\ell n\ [1-\alpha\ t] \tag{56}$$

Thus, the nutation-to-spin-frequency ratio $N(t)/t$ depends on the history of the mass properties from the start of the burn until time t. Of course, before and after the burn, the constant rigid-body values (i.e., $n_0 = I_{z0}\ /I_0 - 1$; $n_f = I_{z\,f}\ /I_f - 1$) should be used.

4.3.3. Evolution of nutation angle

The evolution of the nutation angle $\theta(t)$ during the SRM burn can be expressed in terms of the absolute value of the *complex* planar rotation rate $|\boldsymbol{w}(t)| = \{\omega_x^2 + \omega_y^2\}^{1/2}$ as follows:

$$\begin{aligned}\theta(t) &= \arctan\{I(t)|\boldsymbol{w}(t)|/[I_z(t)\ \Omega]\} \\ &\cong \theta_0\{I(t)/I_0\}\ \{I_z(t)/I_{z0}\}\ \ |\boldsymbol{w}(t)|/|w_0|\end{aligned} \tag{57}$$

Here, the nutation is assumed to remain relatively small.

From Eqs. (47) and (53) we know that $|\boldsymbol{w}(t)| = |\boldsymbol{w}_0|\ [1-\alpha t]^p$ so the nutation damping ratio becomes:

$$\theta(t)/\theta_0 \cong r_I(t)\left[I(t)/I_0\right]^p = r_I(t)|1-\alpha\ t|^p \tag{58}$$

where the constant exponent p is given in Eq. (55a) and the inertia ratio r_I can be calculated as:

$$r_I(t) = \{I(t)/I_0\}/\{I_z(t)/I_z\} = (1-\alpha\ t)/(1-\gamma\ t) \tag{59}$$

Eqs. (58) and (59) reveal the nutation-damping property of the jet-damping torque. Since $I(t)/I_0 < 1$ and $p >> 1$ (e.g., CONTOUR has $p \cong 16$) the nutation decreases exponentially. If the moment of inertia $I(t)$ were to decrease at a slower rate than $I_z(t)$, the ratio $r_I\ (t)$ in Eq. (59) would increase over time and might perhaps compensate the declining effect of $[I(t)/I_0]^p$. In reality, however, $r_I\ (t) < 1$ (e.g., CONTOUR has $r_I \cong 0.97$) or perhaps slightly above 1. In any case, it is extremely unlikely that a relatively small increase in $r_I\ (t)$ might compensate the strong exponential damping effect of the term $[I(t)/I_0]^p$ in Eq. (58).

If a piecewise linear approach is selected, the integration in Eqs. (47) and (48) should be performed with different parameters over each interval $(t_{n-1},\ t_n)$, for $n = 1, \ldots, N$, with $t_0 = 0$ and $t_N = t_f$. By iteration of Eq. (58) we obtain the resulting nutation angle:

$$\theta_n/\theta_0 \cong r_n\left[I_n/I_{n-1}\right]^{p(n)}\ \left[I_{n-1}/I_{n-2}\right]^{p(n-1)}\ \ \ldots\ \ \left[I_1/I_0\right]^{p(1)} \tag{60}$$

with exponents $p(n) = p(t_n)$ and ratio r_n given by:

$$r_n = r_I(t_n) = \{I_n/I_0\}/\{I_{zn}/I_{z0}\} \tag{61}$$

As expected, Eqs. (60) and (61) collapse to Eqs. (58) and (59) in the case when $p(n) = p$ for all n.

4.4. Solution including misalignment torque

When the constant misalignment torque $\mathbf{T}_{thrust}$ of Eq. (43) is also included in Eq. (45) we have:

$$\dot{\boldsymbol{w}} + \{d(t) - j\Omega\ n(t)\}\ \boldsymbol{w} = \boldsymbol{T}/I(t) \tag{62}$$

where $\boldsymbol{T}$ stands for the complex torque parameter (i.e., $\boldsymbol{T} = T_{thrust,x} + j\ T_{thrust,y}$).

Fig. 14 indicates that the rates of change of the three moments of inertia are approximately identical for CONTOUR. Therefore, from here onwards, we restrict ourselves to the special case $\dot{I}(t) \cong \dot{I}_z(t)$. This implies that $\alpha\ I_0 \cong \gamma\ I_{z0}$ and leads to $n(t) \cong n_0\ /(1-\alpha\ t)$ in Eq. (52) and $E \cong n_0$ in Eq. (55b). When substituting $I(t)$ and $d(t)$ from Eqs. (50a) and (51) we can rewrite Eq. (62) as:

$$(1-a\ t)\ \dot{\boldsymbol{w}} + \{d_0 - j\Omega\ n_0\}\ \boldsymbol{w} = \boldsymbol{T}/I_0 \tag{63}$$

The solution $\boldsymbol{w}(t)$ of Eq. (63) with initial condition $\boldsymbol{w}_0 = \boldsymbol{w}(t_0)$ can be written as:

$$\boldsymbol{w}(t) = \boldsymbol{c} + (\boldsymbol{w}_0 - \boldsymbol{c})\ [1-\alpha\ t]^{p-jq} \tag{64}$$

where $p = d_0\ /\alpha$ is the damping parameter and $q = \Omega\ n_0\ /\alpha$ is the frequency parameter. The imaginary constant $\boldsymbol{c}$ is given by:

$$\boldsymbol{c} = \boldsymbol{T}\ (d_0 + j\ \Omega\ n_0)/\left\{I_0(d_0^2 + \Omega^2 n_0^2)\right\} \tag{65}$$

Eq. (64) shows that the solution $\boldsymbol{w}(t)$ describes a circular *spiral* in the complex plane that converges to its centre at point $\boldsymbol{c}$, which is associated with the *tip-off* angle induced by the misalignment torque.

In practice, the magnitude of the imaginary part q of the exponent in Eq. (64) is much larger than that of the real part p (e.g., CONTOUR has $q/p \cong 20$). Therefore, we have $\Omega\ n_0 \gg d_0$ and find the compact approximate result:

$$\boldsymbol{c} \cong j\ \boldsymbol{T}/(I_0\ \Omega\ n_0) \tag{66}$$

This result confirms that the phase angle of the tip-off point is roughly 90° ahead of the phase angle of the misalignment torque. For illustration, the CONTOUR parameters predict a standard deviation of 1.6° for the magnitude of the tip-off angle for a 60-rpm spin rate.

If the misalignment torque $\boldsymbol{T}$ is absent, the vector $\boldsymbol{c}$ in Eq. (66) vanishes and the previous (i.e., jet-damping only) results in Eqs. (47)–(56) are re-established. The rotation

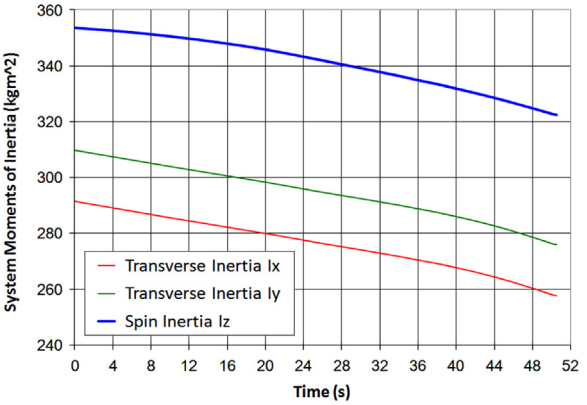

Fig. 14. System moments of inertia during SRM burn.

axis as function of time converges to the origin $\boldsymbol{c}=\boldsymbol{0}$ representing a pure spin without nutation. A *stable* spinner has usually negligible initial nutation and the jet damping will reduce this even further. Also, if the satellite spins about its minor axis the jet-damping effect reduces the nutation in any case.

In the absence of jet damping (e.g., when considering a thrust-misalignment torque during a manoeuvre) the function $d(t)$ as well as the constant α vanish and p, q as well as Eq. (64) become ill-defined. In this case, Eq. (63) shows that the solution corresponds to the well-known motion under a constant body-fixed torque:

$$\boldsymbol{w}(t)=\boldsymbol{c}+(\boldsymbol{w}_0-\boldsymbol{c})\,\exp(j\,\Omega\,n_0\,t) \tag{67}$$

The path of $\boldsymbol{w}(t)$ in the complex plane follows now a *circle* centred at the tip-off point $\boldsymbol{c}$. A visualization of the motion of the angular momentum and delta-velocity vectors for this case may be found in Fig. 2 of Ref. [30].

4.5. Discussion of results

4.5.1. Evolution of mass properties

The evolution of the system mass properties, i.e. mass, moments of inertias, and Centre-of-Mass (CoM) position (measured from the separation plane, see Fig. 12) have been derived from a realistic model for the SRM propellant loss during the SRM burn [7]. The inertias are calculated with respect to the instantaneous system CoM (i.e., satellite, SRM casing, as well as the remaining propellant). From Fig. 14 we know that the evolution of the inertias over the burn starts out close to linear but becomes non-linear near the end of the burn, especially for the transverse inertias.

Fig. 15 shows the displacement of the CoM of the satellite-SRM system during the SRM burn. This result follows by adding the constant mass of the 'empty' satellite to the time-varying mass of the SRM motor consisting of its casing plus propellant. At the start of the burn, the SRM mass is 10% larger than the satellite mass. Therefore, the curve of the system CoM roughly bisects those of the 'empty' satellite and the SRM.

We can understand why the burning of SRM propellant makes the system CoM to first rise and then to fall. Because the propellant starts burning from the SRM bottom upwards, the CoM's of both SRM and system rise initially. After the propellant has burned through the bulge of the SRM its CoM drops and the satellite mass dominates. The movement of the (satellite-SRM) system CoM during the burn leads to a time-dependent behaviour of the jet-damping lever arm ℓ. Its total variation is about 4.6 cm, which is about 5% of its mean value of 1.087 m.

4.5.2. Effect of jet damping

First, we consider the most straightforward jet damping model, i.e. the one based on representative mean values for the relevant parameters *throughout* the SRM burn:

$$\beta=9.186\ \text{kg/s};\quad \alpha=2.26\times10^{-3}\ \text{s}^{-1};\quad y=1.72\times10^{-3}\ \text{s}^{-1} \tag{68a–c}$$

$$n_0=0.1747;\quad p=15.94;\quad q=1.097 \tag{68d–f}$$

The inertia ratio $r_I(t)$ varies between 1.0 at the start and $r_I(t_f)\cong 0.9701$ at the end of the burn with t_f=50.5 s. The final nutation damping can be calculated from Eq. (58):

$$\theta(t_f)/\theta_0=0.1405 \tag{69}$$

Thus, the jet-damping torque reduces the initial nutation by as much as 85.95% at the end of the burn.

Subsequently, we employ the more accurate piecewise linear model in which all parameters are updated at the end of each interval. The 50.5-s SRM burn is divided into 50 intervals of 1 s and the last one of 0.5 s. Fig. 16 shows the corresponding evolutions of the burn rate and the jet damping parameters during the SRM burn. The exponent p shows considerable variations as function of time. These are mainly due to the unsteadiness in the rate of change of the transverse moment of inertia (i.e., α in Eq. (50a), see also Fig. 14). Variations in the mass flow and in the centre of mass movement are less significant.

Fig. 17 shows the evolution of the jet-damping function $d(t)$ and the nutation angle ratio during the SRM burn. The nutation is reduced by as much as 86.49% at the end of the burn. The difference with the result of the preceding straightforward model is only about 0.5%. Therefore, we

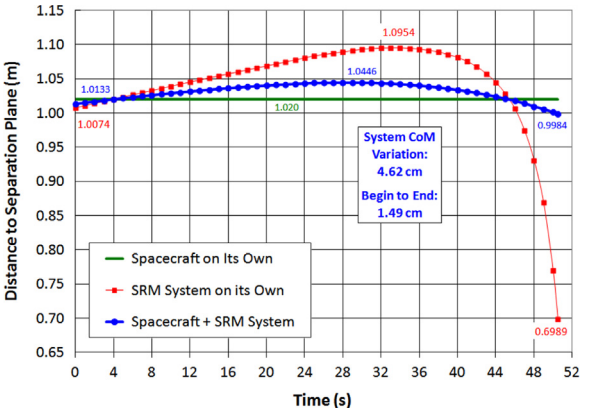

Fig. 15. Evolution of centres of mass during SRM burn.

conclude that the damping effectiveness is *not* at all sensitive to the specific CONTOUR model characteristics.

5. Deep-space navigation lesson

5.1. Background and motivation

ESA uses high-fidelity models for predicting the solar radiation pressure (SRP) forces acting on deep-space satellites. However, significant discrepancies of between 5 and 15% (occasionally even higher) have been observed between estimated and predicted accelerations during the cruise phases of Rosetta, Mars Express, and Venus Express. These discrepancies may be reduced by adding a to-be-estimated SRP scale factor in the satellite-sun direction. While this improves the precision of the main SRP force component, it cannot repair a fundamentally flawed force model in both magnitude *and* direction.

Our work [8–14] has shown that the shortcomings in the SRP modelling can be attributed to forces originating from the thermal radiation re-emitted by the satellite's exterior surfaces. In the special case when the accelerations due to thermal radiation happen to be aligned with those induced by the SRP effects, the SRP scale factors may indeed account for these thermal effects. In general, however, scale factors cannot properly represent the thermally induced acceleration in both magnitude and direction. The replacement of the artificial SRP scale factor by a realistic thermal model enhances the correspondence between the force model and the physical reality. As a consequence, the residuals of the orbit estimation process become smaller in magnitude and look healthier.

5.2. Accelerations induced by thermal radiation

5.2.1. Attitude pointing and control

Fig. 18 shows the Rosetta satellite and its body reference axes. The $+X$ axis points normal to the surface on which the high-gain antenna (HGA) is mounted. The two solar arrays, each having a size of 32.3 m^2, will be extended along the $+Y$ and $-Y$ axes.

Rosetta's attitude is three-axis stabilized during its cruise phases. The attitude control keeps the Sun vector within the first quadrant of the X, Z plane (see Fig. 18) to within a maximum deviation angle of 1° relative to this plane. Thus, the $-X$, $-Z$ surfaces are always in shadow and the $\pm Y$ surfaces barely see the Sun. The arrays rotate about the $\pm Y$ axes and remain oriented normal to the Sun vector for maximum power generation.

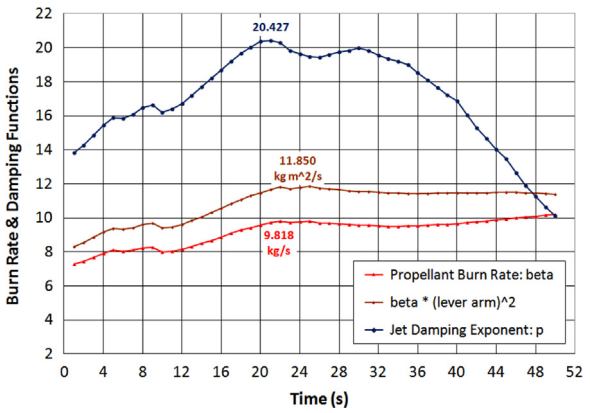

Fig. 16. Evolution of jet-damping parameters during SRM burn.

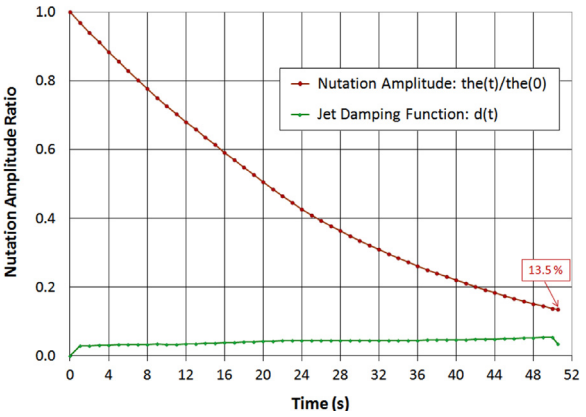

Fig. 17. Effect of jet damping on evolution of nutation angle.

The Sun is the only external thermal radiation source and Rosetta's inertial pointing direction during its cruise phases changes very gradually. Therefore, the temperatures of the exterior surfaces stay essentially constant over a number of days so we may calculate the temperatures from a steady-state heat balance [8].

5.2.2. Heat balance and acceleration due to solar arrays

The incident solar heat flux q_{in} (in W/m^2) that is absorbed by the front side of the solar array is [8]:

$$q_{in} = \alpha_f \frac{S}{d^2} \cos \vartheta \tag{70}$$

where α_f denotes the absorptivity of the array surface, S is the mean Solar Constant of 1366.1 W/m^2 at the satellite's solar distance $d=1$ Astronomical Unit (AU) from the Sun, and ϑ is the solar incidence angle (nominally, $\vartheta \cong 0$).

The heat or energy flux q_{out} that is emitted by a surface at temperature T and emissivity ε is predicted by Stefan–Boltzmann law as:

$$q_{out} = \sigma \varepsilon T^4 \tag{71}$$

where σ denotes the Stefan–Boltzmann constant and T is expressed in units of K.

Fig. 19 shows the heat balance of the incident and re-emitted heat on the front (f) and rear (r) of the solar arrays:

$$q_{in} = q_{f,out} + \ q_{r,out} \tag{72}$$

The re-emitted heat fluxes can be expressed in their respective temperatures T_f and T_r similarly as done in Eq. (71). These temperatures may be calculated [8] from the solar array heat balance and the known conductivity of the honeycomb-aluminium array structure by means of a numerical iteration technique.

The net acceleration in m/s^2 induced by the Lambert-type diffuse thermal emissions from the front and rear

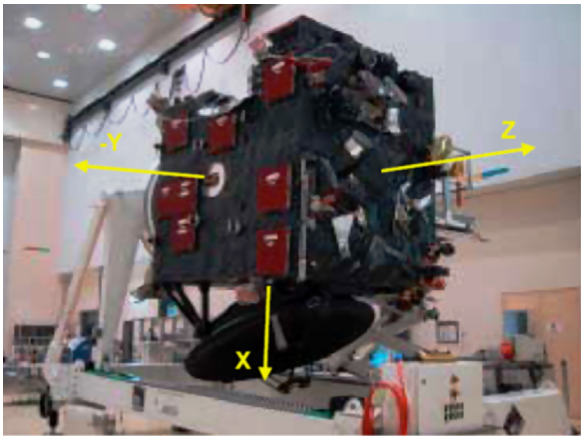

Fig. 18. Rosetta body X, Y, Z reference frame.

solar array (SA) surfaces (see Fig. 19) is given by [8]:

$$\boldsymbol{a}_{TRP,\,SA} = -\frac{2}{3}\frac{\sigma}{c}\frac{A_{SA}}{m}\left(\varepsilon_f\, T_f^4 - \varepsilon_r\, T_r^4\right)_{SA}\boldsymbol{n} \tag{73}$$

where TRP stands for 'Thermal Radiation Pressure', A_{SA} is the surface area of the solar arrays, m is the satellite mass, c is the speed of light, and ε_f and ε_r are the emissivity coefficients of the front and rear solar array panels.

5.2.3. *Heat balance and acceleration due to body surfaces*

We assume that each external body surface element is perfectly insulated from other external surfaces as illustrated in Fig. 20. Heat balances may then be formulated for each surface element individually. The energy transfers *through* the Multi-Layer Isolation (MLI) between cold space and the satellite's interior have been analyzed in detail [9].

The heat balance of the sunlit $+X$ surface may be expressed as:

$$q_{+X,\,in} = \alpha_{MLI}\,\frac{S}{d^2}\,\cos\,\vartheta \approx q_{+X,\mathrm{out}} \tag{74}$$

where α_{MLI} is the absorptivity of the outer MLI sheet. The exterior temperature T_{+X} follows again from Stefan–Boltzmann law as in Eq. (71) but is now based on the emissivity ε_{MLI}. For the solar distance $d=1$ AU and incidence angle $\vartheta=0^\circ$ we obtain [9] $T_{+X}=129$ °C.

The temperature of the shadowed $-X$ surface can be calculated [9] from the expected 5 W/m^2 heat transfer from the warm satellite interior at about 20 °C through the MLI sheets into cold deep space at 3 K. Its value at the solar distance 1 AU can be calculated to be $T_{-X}=-172$ °C.

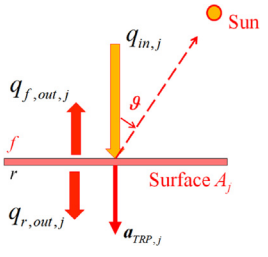

Fig. 19. Heat balance and TRP acceleration on an arbitrary surface A_j.

The acceleration in m/s^2 resulting from the thermal emissions by the $+X$ and $-X$ surfaces can be calculated similarly as was done for the solar arrays in Eq. (73):

$$\boldsymbol{a}_{TRP,X} = -\frac{2}{3}\frac{\sigma A_X}{c\,m}\,\varepsilon_{MLI}\left(T_{+X}^4 - T_{-X}^4\right)\boldsymbol{X} \tag{75}$$

where $\boldsymbol{X}$ is the unit-vector along the $+X$ axis. Similar results can be found for the $+Z$ and $-Z$ surfaces with incidence angle $\vartheta=90^\circ$. The temperature difference for the body surfaces, i.e. $T_{+X}-T_{-X}\cong 300$ °C, which is 20 times larger than $T_f-T_r\cong 15$ °C for the solar arrays (all evaluated at 1 AU solar distance). As a consequence, the body's thermal acceleration is in fact slightly larger than the acceleration induced by the much larger arrays [8,9].

Precise high-fidelity analytical SRP and TRP models have been established by Kato et al. [10,11]. These models account for the actual in-flight pointing history (expressed in elevation and azimuth angles) of Rosetta's High-Gain Antenna (HGA) during the cruise phases. The HGA's contributions to the SRP and TRP accelerations are of the order of 3% to 5%.

Further enhancements in the level of geometric precision and overall modelling fidelity may be achieved by using a numerical technique similar to the finite-element method [12]. This approach uses detailed discretisations of the satellite surfaces. By computing the effects for each individual surface element, the resulting forces and torques acting on the satellite can be modelled very precisely. The achievable accuracy is limited only by the discretization mesh size and by the computing power.

5.3. *Sample of results for Rosetta*

The thermal-model predictions of the non-gravitational forces have been compared with the observed ones derived from ESOC's state estimates [13], see Fig. 21. The blue line represents the percentage error of the predictions when the SRP is taken as the sole non-gravitational force. The green line shows the percentage error when both SRP and TRP forces are considered. The significant improvement can easily be observed.

Similar results are obtained for the later Rosetta cruise phases and also for the Mars Express and Venus Express cruise phases. Overall, the SRP plus thermal models account for 97 to 99% of the observed non-gravitational accelerations.

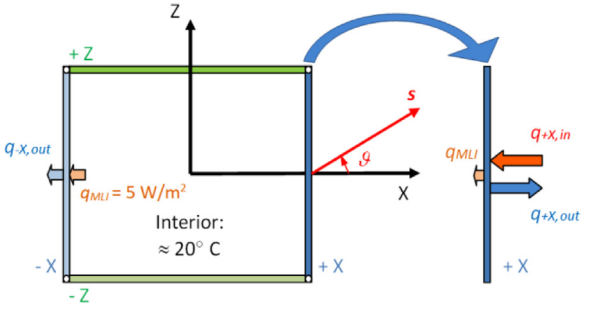

Fig. 20. Configuration of satellite body surfaces [9].

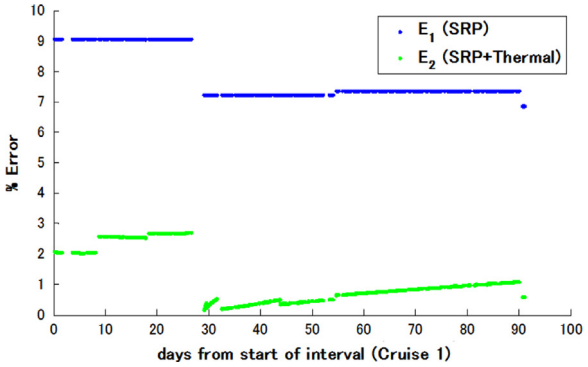

Fig. 21. Errors in modelling of non-gravitational forces [13].

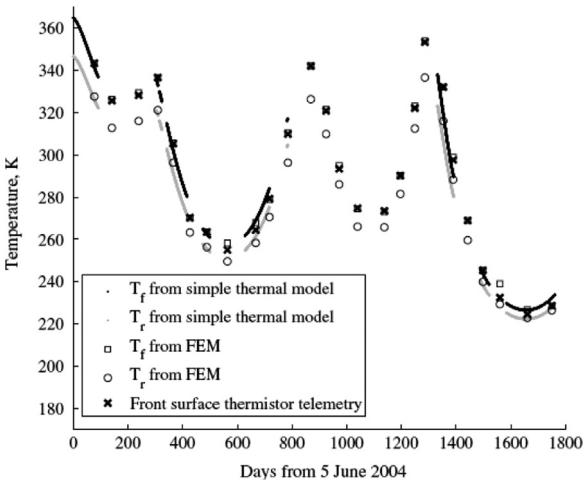

Fig. 22. Comparison of solar-array temperatures for Rosetta [13].

Fig. 22 shows the comparisons of the solar-array temperature predictions from our straightforward model with those obtained by a finite-element method and with actual thermistor telemetry readings from the solar array.

5.4. *Venus Express temperature comparisons*

Venus Express (VEX) has thermistors on the rear of its solar arrays. Their temperature readings have been compared with our predictions for the rear of the solar arrays. The two data sets showed systematic offsets of between 8 and 16 °C. These discrepancies are due to the fact that part of the power generated by the arrays is used for on-board consumption. Therefore, it makes sense to exclude the converted power from the initial heat input q_{in} when predicting the array temperatures during the simulations. Fortunately, reliable data on the level of converted power are provided in the telemetry.

Another issue is the fact that the efficiency of the solar-cells decreases with higher temperatures (and this dominates the degradation due to aging effects for VEX). Therefore, a linear model [14] was constructed for modelling the cell efficiency as a function of solar distance between 1.0 and 0.7 AU.

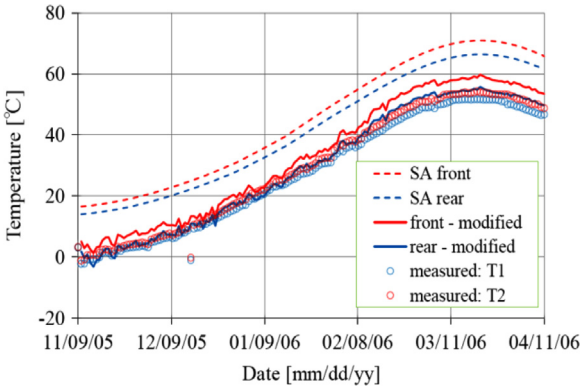

Fig. 23. Comparison of predicted and measured solar array temperatures for Venus Express [14].

Fig. 23 shows the comparison of the measured and predicted temperatures with adjustments for the power conversion effect and for the degradation of the solar cell efficiency. The efficiency at 0.7 AU is taken as 95% of the one at 1 AU. The red and blue lines represent the adjusted temperatures whereas the dashed lines are those without adjustments. The continuous blue curve shows excellent agreements with the blue and red circular markers, which represent the actual in-flight temperature readings for each of the two solar arrays.

6. Conclusion

The paper presents interesting and valuable insights offered by unexpected flight-dynamical performances of orbiting satellites. These lessons demonstrate that the evaluation of in-flight performances offers unique opportunities for enhancing our understanding of satellite dynamics for operational as well as educational benefits.

Acknowledgements

The author acknowledges his colleagues and friends for sharing their valuable expertise and insights. Frank Janssens's gift for solving intricate satellite dynamics problems is admirable as well as inspirational. George Koppenwallner's expertise and enthusiasm were crucial for my edification in the field of free-molecular flow. Many thanks go to Robert Farquhar, David Dunham, and Wayne Dellinger for the productive and pleasant atmosphere during the CONTOUR project. The author is grateful to Trevor Morley for expert guidance during our study on the Rosetta navigation issues. Last but not least, the author acknowledges the devoted efforts of Takahiro Kato, Michael Shoemaker, Kikuko Miyata, Yoshihide Sugimoto, and Benny Rievers during this study.

References

[1] J.C. van der Ha, John V. Breakwell: astrodynamicist and friend, Acta Astronaut. 29 (6) (1993) 481–483.

[2] K.C. Howell, R.W. Farquhar, John Breakwell, the restricted problem, and Halo orbits, Acta Astronaut. 29 (6) (1993) 485–488.
[3] J.-P. Marec, John V. Breakwell and optimization, Acta Astronaut. 29 (6) (1993) 489–496.
[4] Ph. Boland, F. Janssens, The GEOS-1 dynamic experiment, ESA J. 3 (3) (1979) 265–280.
[5] J.C. van der Ha, Attitude perturbations induced by free-molecular flow interactions in perigee region, Acta Astronautica 13 (6–7) (1986) 301–309.
[6] J.C. van der Ha, Approximate free-molecular flow torques on spinning satellites, J. Astronaut. Sci. 34 (4) (1986) 403–419.
[7] J.C. van der Ha, F. L Janssens, Jet damping and misalignment effects during SRM burn, J. Guid. Control Dyn. 28 (3) (2005) 412–420.
[8] J.C. van der Ha, D. Stramaccioni, Thermal radiation effects on deep-space trajectories, Adv. Astronaut. Sci. 136 (2010) 1861–1880. (Spaceflight Mechanics 2010).
[9] J.C. van der Ha, Comparison of solar and thermal radiation accelerations of deep-space satellites, Adv. Astronaut. Sci. 152 (2014) 2727–2746. (Space Flight Mechanics 2014).
[10] T. Kato, J.C. van der Ha, Precise modeling of solar and thermal accelerations on Rosetta, Acta Astronaut. 72 (2012) 165–177.
[11] T. Kato, B. Rievers, J.C. van der Ha, C. Laemmerzahl, Detailed analysis of solar and thermal accelerations on deep-space satellites, Adv. Astronaut. Sci. 143 (2012) 1761–1776. (Space Flight Mechanics 2012).
[12] B. Rievers, T. Kato, J.C. van der Ha, C. Laemmerzahl, Numerical prediction of satellite surface forces with application to Rosetta, Adv. Astronaut. Sci. 143 (2012) 1123–1142. (Space Flight Mechanics 2012).
[13] M. Shoemaker, J.C. van der Ha, T. Morley, Modeling and Validation of Thermal Radiation Acceleration on Interplanetary Spacecraft, J. Spacecr. Rockets 49 (2) (2012) 212–219.
[14] Y. Sugimoto and J. C. van der Ha. Thermal radiation modelling for interplanetary spacecraft orbit propagation, in: Proceedings of the 28-th International Symposium on Space Technology and Science, Okinawa, Japan, June 5–12, 2011, Paper ISTS-2011-d-57.
[15] J.C. van der Ha, Perturbation solution of attitude motion under body-fixed torques, Acta Astronaut. 12 (10) (1985) 861–869.
[16] J. C. van der Ha. Optimisation of HIPPARCOS Gyro Configuration, ESOC/ OAD Working Paper No. 238, European Space Agency, October, 1983.
[17] G. Koppenwallner. Freimolekulare Aerodynamik für Satellitenanwendung, DFVLR FB-82-08, Deutsche Forschungs & Versuchsanstalt für Luft- und Raumfahrt, Göttingen, Germany, January, 1982.
[18] R.D. Boettcher, H. Legge, Determination of aerodynamic forces on satellites by theory and wind tunnel experiments, Acta Astronaut. 7 (4–5) (1980) 255–267.
[19] R. D. Boettcher. Analysis of Free Molecular Effects on the Attitude of Satellites in Geostationary Transfer Orbit; Part I: Theoretical Analysis, DFVLR IB-222-86-A-08, Deutsche Forschungs- und Versuchsanstalt für Luft- und Raumfahrt, Göttingen, Germany, 1986; also: ESA-CR(P) 2408, 1986.
[20] G. Koppenwallner and H. Legge. Analysis of Free Molecular Effects on the Attitude of Satellites in Geostationary Transfer Orbit; Part II: Force and Torque Measurement in Free Molecular Wind Tunnel Tests', DFVLR IB-222-86-A-07, Deutsche Forschungs- und Versuchsanstalt für Luft- und Raumfahrt, Göttingen, Germany, 1986; also: ESA-CR(P) 2408, 1986.
[21] H. Klinkrad and B. Fritsche. Orbit and attitude perturbations due to aerodynamics and radiation pressure, ESA Workshop on Space Weather, ESA-WPP-155, 11–13 November 1998, ESA/ESTEC, Noordwijk, the Netherlands.
[22] K. Moe, M.M. Moe, Gas-surface interactions and satellite drag coefficients, Planet. Space Sci. 53 (8) (2005) 793–801.
[23] J. C. van der Ha. Free-molecular flow induced attitude changes of spinning satellites in elliptical orbits, (Space Flight Mechanics 2013), Adv. Astronaut. Sci., vol. 148, pp. 1321–1340.
[24] D. King-Hele, Theory of Satellite Orbits in an Atmosphere, Butterworths, London, 1964.
[25] J.A. Wertz, W.L. Larson (Eds.), Space Mission Analysis and Design, 2nd edition, Microcosm, Inc., Torrance, CA, and Kluwer Academic Publishers, Dordrecht, The Netherlands, 1992, pp. 206–212.
[26] D.W. Dunham, D.P. Muhonen, R.W. Farquhar, M. Holdridge, E. Reynolds, Design and implementation of CONTOUR's phasing orbits, Adv. Astronaut. Sci. 114 (Part II) (2003) 1535–1547. (Spaceflight Mechanics 2003).
[27] J.C. van der Ha, G. Rogers, W. Dellinger, J. Stratton, CONTOUR phasing orbits: attitude determination & control concepts & flight results, Adv. Astronaut. Sci. 114 (Part II) (2003) 767–781. (Spaceflight Mechanics 2003).
[28] R.W. Farquhar, Fifty Years on the Space Frontier: Halo Orbits, Comets, Asteroids, and More, Outskirts Press, Inc., Denver, CO, 2011.
[29] F. Janssens, Jet damping and nutation growth during the burn of a solid rocket motor such as PAM-D, ESA J. 12 (3) (1988) 273–288.
[30] J.A. Oldenburg, S.G. Tragesser, Minimizing the effects of transverse torques during thrusting for spin-stabilized spacecraft, J. Guid. Control Dyn. 25 (3) (2002) 591–595.